PHYSICAL REVIEW B, VOLUME 65, 165308

Probing the quantum states of self-assembled InAs dots by magnetotunneling spectroscopy

A. Patanè, R. J. A. Hill, L. Eaves, P. C. Main, M. Henini, M. L. Zambrano,* and A. Levin
School of Physics and Astronomy, University of Nottingham, Nottingham NG7 2RD, United Kingdom

N. Mori and C. Hamaguchi
Dept. of Electronic Engineering, University of Osaka, 2-1 Yamada-Oka, Suita City, Osaka 565-0871, Japan

Yu. V. Dubrovskii and E. E. Vdovin
Institute of Microelectronics Technology RAS, 142432 Chernogolovka, Russia

D. G. Austing
NTT Basic Research Laboratories, NTT Corporation, 3-1 Morinosato, Wakamiya, Atsugi, Kanagawa 243-0198, Japan

S. Tarucha
Department of Physics, University of Tokyo, 7-3-1 Hongo, Bunkyo-ku, Tokyo 113-0033, Japan;
NTT Basic Research Laboratories, NTT Corporation, 3-1 Morinosato, Wakamiya, Atsugi, Kanagawa 243-0198, Japan;
and ERATO Mesoscopic Correlation Project, NTT Basic Research Laboratories, 3-1 Morinosato, Wakamiya, Atsugi, Kanagawa 243-0198, Japan

G. Hill
Dept. of Electronic and Electrical Engineering, University of Sheffield, S3 3JD Sheffield, United Kingdom

(Received 2 November 2001; published 4 April 2002)

We describe how magnetotunneling spectroscopy can be used to investigate the spatial form of the wave function of confined electron states in self-assembled InAs quantum dots grown on (100)- and (311)B-oriented GaAs substrates. For both orientations, the wave function is found to have a biaxial symmetry in the growth plane, with axes parallel to the main crystallographic directions. We also present magnetotunneling spectroscopy measurements in a multiple-terminal resonant-tunneling device, which incorporates a series of gate electrodes. The gates allow us to address an individual dot electrostatically, and to identify and measure its energy levels and associated wave functions. The limitations and possible future applications of the technique are also discussed.

DOI: 10.1103/PhysRevB.65.165308 PACS number(s): 73.63.−b, 73.63.Kv, 73.43.Jn

I. INTRODUCTION

During the last few years there has been continuous and increasing interest in imaging the quantum environment of electrons and atoms. In particular, various scanning probe techniques, such as scanning tunneling microscopy (STM) (Refs. 1–3) and scanning single-electron transistor microscopy[4,5] have been used successfully to probe atoms or electron charge distributions in a wide variety of systems, including metals and superconducting materials. This raises the question of whether it is also possible to image the electron wave function in a quantum dot (QD), an artificial nanometer-sized cluster, which confines the motion of an electron in all three spatial dimensions.[6–19] In a QD, electrons are confined to length scales of ~10 nm, and their behavior is characterized by quantum-mechanical effects, such as the formation of an atomlike, discrete energy-level spectrum.

In principle, it is possible to investigate the probability density of electrons in a QD using a surface probe technique such as STM. This is a powerful tool for imaging the electronic states of dots near a surface,[20,21] but a different approach is required for dots incorporated into real semiconductor devices, where the dots may be buried hundreds of nanometers below the surface. Two recent papers have reported the imaging of wave functions associated with QD's.[22,23] In the first experiment,[22] a cross-sectional STM of cleaved InAs/GaAs self-assembled QD's was used to probe the profile of the electron density along the plane of vertical confinement of the dot (i.e., along the growth direction and one in-plane direction). However, since the measured wave patterns probably arose from a superposition of the probability densities of the electron ground and excited states, the technique did not allow the various confined states of the dot to be distinguished clearly. In addition, this method is both invasive and destructive, as the QD is cleaved into two pieces. In the second experiment,[23] we showed that magnetotunneling spectroscopy (MTS) (Refs. 24–26) provides a nondestructive and noninvasive method of probing the electron wave function of a QD. The technique exploits the effect of the classical Lorentz force on the motion of an electron tunneling into the QD, and can be regarded as the momentum- (**k**-) space analogue of STM imaging. In STM, a moving tip acts as a probe of the wave function in real space. In MTS, the applied magnetic field B acts as a variable probe in **k** space: the images give the probability density in **k** space of the electron wave function.

In this work, we apply the MTS technique to probe the

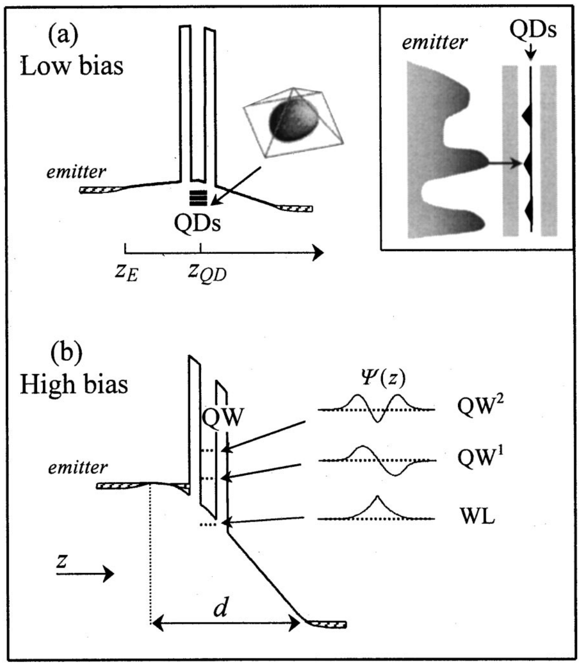

FIG. 1. Schematic conduction band profile of a GaAs/Al$_x$Ga$_{1-x}$As resonant tunneling diode with InAs quantum dots (QD's) and a wetting layer (WL) incorporated in a GaAs quantum well (QW) in the regime of (a) low- and (b) high-bias conditions (devices of type A). Electrons tunnel from the emitter into (a) the QD states and into (b) the WL, and confined subbands QW^1 and QW^2 of the QW. The inset shows a sketch of electrons tunneling from a "finger-like" distribution of occupied states in the emitter into the QD's.

electron-confined states of self-assembled InAs QD's incorporated in two-terminal tunnel devices grown on (311)*B*- and (100)-oriented GaAs substrates. We also show that the MTS technique can be refined further by using devices that incorporate an array of gate electrodes: the gate-technology provides a means of electrostatically addressing an individual dot, and thus allows us to identify and measure its energy levels and wave functions.

The paper is organized as follows. In Sec. II, we describe the growth conditions and compositional structure of our samples. Section III describes the electrical characteristics of the devices. In Secs. IV and V we present the MTS data, and describe how these provide detailed information about the shape and orientation of the electron wave function confined in dots grown on differently oriented GaAs substrates. Also, as a means of validating the MTS technique, we examine the spatial symmetry of the electron wave function associated with hydrogenic donor states. In Sec. VI, we describe how an array of gate electrodes provides us with a means of controlling the electrostatic profile in a layer of QD's. In combination with magnetotunneling spectroscopy, this allows us to identify and measure both the energy levels and wave functions associated with the ground and excited state of an individual dot. The paper concludes with a discussion of the limitations (Sec. VII) and possible future applications of the technique (Sec. VIII).

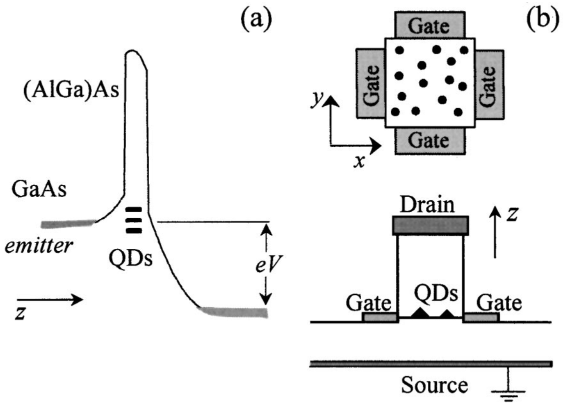

FIG. 2. (a) Schematic conduction-band profile of a single-barrier GaAs/Al$_x$Ga$_{1-x}$As tunneling device (TD) with InAs quantum dots (QD's) incorporated in a Al$_x$Ga$_{1-x}$As barrier (device B). (b) Schematic diagram of a TD with multiple-gate electrodes.

II. SAMPLES

Our devices were grown by molecular-beam epitaxy. We consider two types of structure, which we label types A and B. For type A devices, a layer of InAs QD's is embedded in the center of an undoped 12-nm GaAs quantum well (QW), which is sandwiched between two 8.3-nm Al$_{0.4}$Ga$_{0.6}$As tunnel barriers, as shown in Fig. 1. Undoped GaAs spacer layers of width 50 nm separate the Al$_{0.4}$Ga$_{0.6}$As barriers from $2\times10^{17}\mathrm{cm}^{-3}$ *n*-doped GaAs layers of width 50 nm. Finally, $3\times10^{18}\mathrm{cm}^{-3}$ *n*-doped GaAs layers of width 0.3 μm were used to form electrical contacts. Here we focus on two type-A structures, one grown on a (311)*B*-oriented GaAs substrate (sample A1) and the other on a (100)-oriented GaAs substrate (sample A2). These structures were grown at 600 °C except for the InAs layer and the overgrown GaAs barrier, which were grown at 480 °C. For comparison, we also studied a series of control samples. Two samples were grown with the same sequence of layers as that described above, except that one has only a thin InAs two-dimensional wetting layer (i.e., containing no QD's, sample C1) and the other has no InAs layer at all (sample C2). The third control sample is an Al$_{0.4}$Ga$_{0.6}$As/GaAs/Al$_{0.4}$Ga$_{0.6}$As tunneling diode in which the central plane of the quantum well was lightly doped with $4\times10^{9}\mathrm{cm}^{-2}$ Si donors (sample C3).[26] The samples were processed into circular mesa structures of diameter between 10 and 200 μm, with Ohmic contacts alloyed to the doped regions. For the type-B structure, a single InAs QD layer was incorporated in the center of a 14-nm-thick Al$_{0.2}$Ga$_{0.8}$As tunneling barrier, as shown in Fig. 2(a). Undoped GaAs spacer layers of width 3 nm separate the Al$_{0.2}$Ga$_{0.8}$As barrier from *n*-doped GaAs layers in which the doping concentration increases in steps from 1×10^{17} cm^{-3}, close to the barrier, to 2×10^{18} cm^{-3}. Growth temperatures for the InAs layer and the other layers were 520 and 550 °C, respectively. Sample B was grown on a (311)*B*-oriented GaAs substrate. It was processed into a square mesa of side length 0.7 μm. It incorporates four independent, lateral gates in addition to the source and drain contacts [see Fig. 2(b)]. The source-drain voltage, *V*, and the gate voltage, V_g, were measured relative to the source substrate contact.

III. TUNNELING THROUGH SELF-ASSEMBLED QUANTUM DOTS

We first consider type-A structures, in which the dots are embedded in the central plane of a GaAs/$\mathrm{Al}_x\mathrm{Ga}_{1-x}\mathrm{As}$ QW. Recently, we showed that a thin pseudomorphic InAs layer [wetting layer (WL)] incorporated in the central plane leads to a significant lowering of the energy of the quasi-two dimensional ground-state subband of the QW.[27] Above a critical WL thickness, QD's are formed. This further modifies the electronic states of the system: first, the dots give rise to discrete zero-dimensional bound states below the GaAs conduction-band edge and, second, they create a considerable amount of disorder, which influences the properties of the continuum of the subband states and the electron tunneling dynamics.[28]

Figures 1(a) and 1(b) show the conduction-band potential profile for devices of type A, in two different regimes of bias. At zero bias, equilibrium is established by electrons diffusing from the doped GaAs layers into the dot states, which lie below the GaAs conduction-band edge.[27] This negative charge in the well produces two depletion layers in the regions beyond the $\mathrm{Al}_x\mathrm{Ga}_{1-x}\mathrm{As}$ barriers. When a small voltage V is applied [Fig. 1(a)], resonant tunneling through a particular QD state leads to a resonance in $I(V)$, whenever the energy of the QD state is resonant with an adjacent filled state in the negatively biased electron emitter layer. For sufficiently high bias voltages [Fig. 1(b)], electrons can tunnel through the WL states and the confined subbands of the QW. A detailed discussion of this high-bias regime was reported in Ref. 27. In the following we focus on the low-bias regime related to resonant tunneling into the dot states.

Despite the large number of quantum dots in a typical sample (10^6-10^7 for a 100-μm-diameter mesa), we observe only a small number of strong resonant peaks in the low bias ($|V|<0.2$ V) $I(V)$ curve. The observation of a small number of resonant current peaks in mesas containing a large ensemble of QD's was also reported in earlier studies.[29–34] This result is surprising at first sight. We propose that this behavior is partially related to the fact that only a limited number of conducting channels can efficiently transmit electrons from the doped layer to quantum dots at low bias. Note that the transport of electrons from the heavily doped contact layers through the more lightly doped regions into the tunnel barrier and QD layers is influenced by the local and random distribution of donor impurities and/or residual strain and by charging of the QD's. In particular, we expect that in some areas of the device the electron ‘‘Fermi sea’’ extends out toward the dot layer, thus producing ‘‘finger-like’’ protrusions of occupied electron states, as shown schematically in the inset of Fig. 1. Since the tunnel current depends exponentially on the tunneling distance, those dots that are closer to one of the ‘‘fingers’’ are preferentially selected for tunneling, and produce the strongest resonant features in the $I(V)$ characteristic. Also, closer inspection of the $I(V)$ curves reveal that, in addition to the strong peaks that we consider in this paper, there are weaker features and a background current. We believe that these arise from tunneling through the ensemble of dot states, most of which have larger tunneling distances and correspondingly lower tunnel currents. This implies that the strong peaks in $I(V)$ correspond to only a small selection of dots out of the full QD distribution.

The average separation, d, between the edges of the electron distributions in the emitter and collector [see Fig. 1(b)] can be determined by capacitance-voltage, $C(V)$, measurements. We model the tunneling diode as a parallel-plate capacitor, and express the capacitance as $\kappa\kappa_0 A/d$, where κ is the relative permittivity constant of GaAs ($\kappa=12.8$) and A is the area of our 100-μm-diameter mesa. Using a typical value of the capacitance ($C\sim16$ pF) measured at low bias ($|V|<0.1$ V),[27] we find that $d\sim56$ nm. In turn, this provides an estimate for the average tunneling distance Δs of the electron from the emitter (collector) to the dot layer, which is equal to $d/2\sim28$ nm. Due to the likely presence of electron ‘‘fingers’’ in the emitter, the effective tunneling distance for the more intense QD resonances in $I(V)$ is likely to be smaller than this estimate. However, the structure of the device indicates that Δs cannot be much less than ~20 nm, since the sum of the barrier width plus the half-width of the GaAs well is 14 nm, and we also need to take into account the finite spread (~10 nm) of the electron wave function in the emitter region adjacent to the $\mathrm{Al}_x\mathrm{Ga}_{1-x}\mathrm{As}$ barrier.

Figure 3(a) shows the $I(V)$ characteristic in reverse bias (positive biased substrate) for sample A1 in the low-bias regime. Resonances in the current are observed in a voltage range from 0 to -0.2 V, and are superimposed on a rising background. These resonances are not observed in the two control samples, which indicates that they are related directly to the presence of the dots, while the background current is probably due to tunneling through the ensemble of dot states.

We have carried out a detailed study of the temperature dependence of the $I(V)$ curve. This indicates that the peaks in $I(V)$ are due to tunneling through individual QD's. With decreasing temperature from 2 to 0.3 K, a thermally activated current onset is observed for each resonant feature. This is shown in the inset of Fig. 3(a), which plots the $I(V)$ characteristic on a log(I) scale over a narrow range of voltage. The observation of a thermally activated current onset down to temperatures as low as 0.3 K suggests that each current feature is due to resonant tunneling through a discrete state of an individual dot. A current onset is observed when the energy level of the zero-dimensional state of the QD coincides with the Fermi energy of electrons in the emitter. As we lower the temperature, we find that the threshold region for current increase becomes more sharply defined, and is limited only by the k_BT smearing of the emitter Fermi level. Such a behavior reflects the characteristic property of an electron tunneling process from a thermalized Fermi distribution of emitter states into an individual and discrete zero-dimensional state.[34,35] We attribute the broad and composite structure of each resonance [see the resonance in the inset of Fig. 3(a)] to mesoscopic fluctuations of the local density of electron states in the emitter: as the bias voltage is varied, the QD level scans the energy range of the states below the Fermi energy in the emitter.[35]

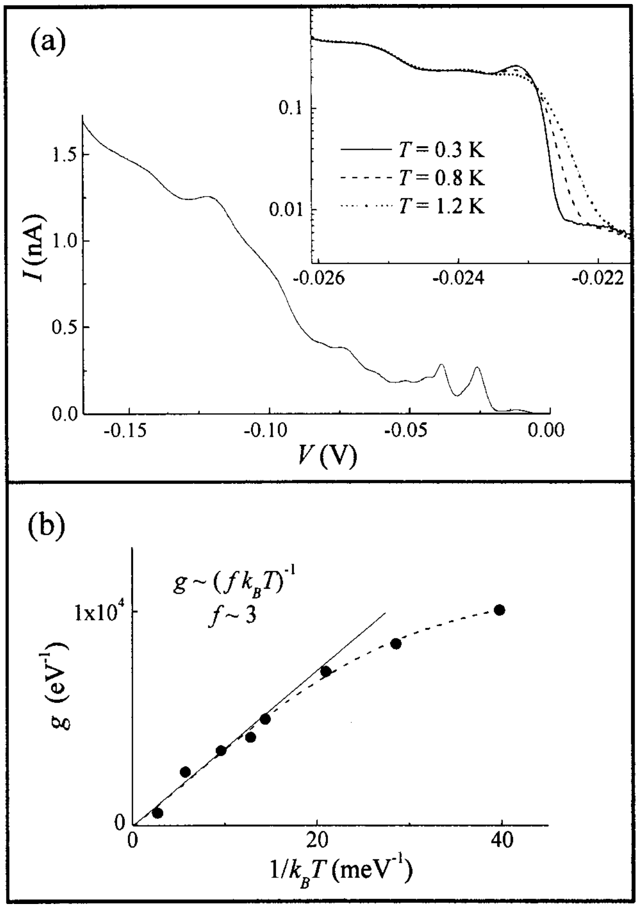

FIG. 3. (a) Low-temperature $I(V)$ characteristic of device A1 at $T = 4.2$ K. The inset shows the temperature dependence of the onset of a typical resonant current feature. (b) Derivative

$$g = \frac{1}{e}\frac{d[\ln(I)]}{dV},$$

estimated at the onset of the resonant feature shown in (a), vs the reciprocal of thermal energy $k_B T$. The dashed line is a guide to the eye. The continuous line is a linear fit to the six highest temperature points of the plot with slope $1/f$, where f is the electrostatic leverage factor.

The temperature dependence of the current onset allows us to determine the electrostatic leverage factor f, which relates the applied voltage V to the energy of the dot, ε, measured relative to the Fermi energy in the emitter ($f \sim eV/\varepsilon$). The tunneling current into a dot state of energy ε is proportional to $\exp(-\varepsilon/k_B T) \sim \exp(-eV/f k_B T)$. This implies that a plot of $\ln(I)$ versus eV should be described by a straight line with a gradient, g, given by $(f k_B T)^{-1}$. The leverage factor can then be derived by the reciprocal of the slope of the measured values of g versus $(k_B T)^{-1}$ [see Fig. 3(b)]. For the higher temperatures (>0.6 K), g follows a straight line from which we obtain $f = 3.0 \pm 0.2$. In contrast, at low bath temperatures (<0.4 K), g departs from a linear dependence, probably due to a saturation of the temperature of the electrons in the emitter at ~0.4 K. A leverage factor of 3 is also consistent with a simple electrostatic model of the device.

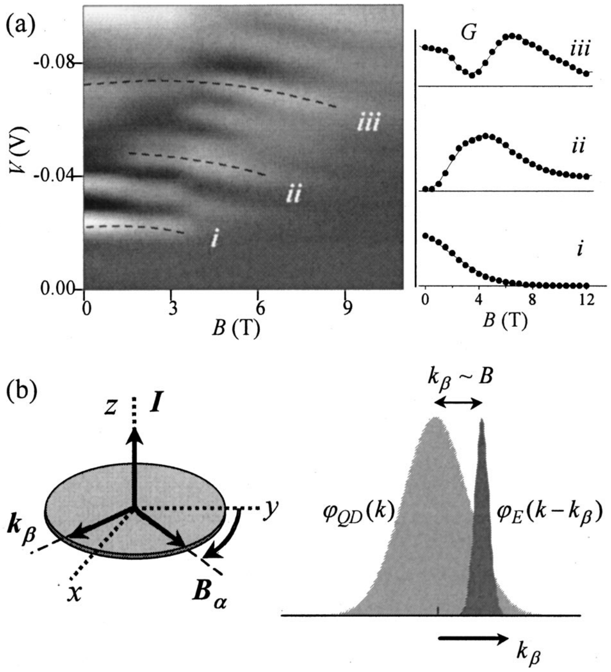

FIG. 4. (a) Gray-scale plot of the differential conductance $G = dI/dV$ for device A1 at $T = 4.2$ K with axes of voltage V and magnetic field B. Lighter shades represent higher values of G. Dashed lines indicate three conductance resonances labeled *i*, *ii*, and *iii*. The right inset shows the B dependence of the amplitude of the conductance peaks associated with *i*, *ii*, and *iii*. (b) Left: sketch of the geometry of our magneto-tunneling experiment: α, β, and z indicate, respectively, the direction of B, the direction of the in-plane wave vector k_β, acquired by the electron due to the action of the Lorentz force, and the direction of the current, respectively. Right: overlap between $\varphi_E(k-k_\beta)$ and $\varphi_{\mathrm{QD}}(k)$, the Fourier transforms associated with the electron wave function in the emitter and quantum dot, respectively, for a given magnetic field. As the tunnel current is given by the square of the overlap integral of the two functions, varying B and hence k_β allows us to determine the form of $\varphi_{\mathrm{QD}}(k)$.

IV. MAGNETOTUNNELING SPECTROSCOPY

In this section, we focus on the magnetic field dependence of the current resonances associated with the dots, and on how this provides detailed information on the form of the wave function associated with an electron in a QD. Figure 4(a) shows the gray-scale plot of the differential conductance, $G(B) = dI/dV$, for sample A1 at $T = 4.2$ K as a function of applied voltage and magnetic field, B. The direction of B is perpendicular to the current flow. Lighter shading represents higher values of G. We use a $G(B)$ plot rather than an $I(B)$ plot since the differential conductance allows us to identify the onset of the resonance due to each QD, and to determine more clearly the magnetic field dependence of each resonant feature. However, the B dependence of the measured values of the current or of the integrated current over a particular feature, $\int_{\mathrm{peak}} I(V)\,dV$, are quantitatively similar.

The figure shows clearly that the intensity of the conductance resonances depends strongly on B. Three resonances are indicated, *i*, *ii*, and *iii*, corresponding to current features that show behavior typical of a large number of samples that we have studied. Resonance *i* shows a maximum in $G(B)$ at $B=0$ T, followed by a steady decay to zero at around 6 T; resonance *ii* shows almost no conductance at $B=0$ T, with $G(B)$ increasing to a broad maximum at ~ 5 T, followed by a gradual decay towards zero; resonance *iii* shows two clear maxima in G at $B=0$ and ~ 7 T, with $G(B)$ falling to a minimum value of almost zero between these maxima. The amplitude of all peaks is quenched at high field.

We can understand qualitatively the magnetic field dependence of the resonances in terms of the effect of B on a tunneling electron. Let α, β, and z indicate the direction of B, the direction normal to B in the growth plane (x,y), and the direction normal to the tunnel barrier, respectively [see Fig. 4(b)]. When an electron tunnels from the emitter into the dot, it acquires an additional in-plane momentum given by $k_\beta = eB\Delta s/\hbar$, where Δs is the effective distance tunneled along z from the emitter to a QD. We envisage the tunneling into the QD as a ballistic process in which no scattering occurs. This is a reasonable assumption as the density of ionized impurities in the undoped emitter spacer layer, barrier and quantum-well regions is very low ($<10^{15}\ \mathrm{cm}^{-3}$). The effect of the magnetic field can be understood semiclassically in terms of the increased momentum along β that is acquired by the tunneling electron due to the action of the Lorentz force. The applied voltage allows us to tune resonantly to the energy of a particular QD state. Then, by measuring the variation of the tunnel current with B, we can determine the size of the matrix element that governs the quantum transition of an electron as it tunnels from a state in the emitter layer into a QD.

In order to analyze the results of our experiment, we express the tunneling matrix element M in terms of the Fourier transforms $\varphi_{i(f)}(k)$, of the conventional real-space wave functions, according to the relation $M=\int_k \varphi_i(k-k_\beta)\varphi_f(k)dk$, and express the tunnel current as $I\sim|M|^2$.[25,26] Here the subscripts i and f indicate the initial (emitter E) and final (quantum dot QD) states of the tunnel transition. Relative to the strong spatial confinement in the QD, the initial state in the emitter has only weak spatial confinement. Hence, in k-space, $\varphi_i(k-k_\beta)$ corresponds to a sharply peaked function with a finite value only close to $k=k_\beta$. In contrast, for the spatially confined QD state, $\varphi_f(k)$ is spread over a wide range of k. As the tunnel current is given by the square of $M(k_\beta)$, the narrow spread of k for $\varphi_E(k-k_\beta)$ allows us to determine the form of $\varphi_{\mathrm{QD}}(k)$ by varying B and hence k_β [see Fig. 4(b)]. In particular, if $\varphi_E(k-k_\beta)$ is approximated by a δ function, then $M(k_\beta)$ is equal to $\varphi_{\mathrm{QD}}(k_\beta)$. A more detailed account of our model of the tunneling process in given in the Appendix.

The model provides a simple explanation of the magnetic field dependence of the resonant current features *i*, *ii*, and *iii*. The $I(B)$ or $G(B)$ plot associated with these resonances describes the form in k space of the wave function probability density $|\varphi_{\mathrm{QD}}(k_\beta)|^2$, associated with different types of dot states, i.e., the ground (*i*) state and first (*ii*) and second (*iii*) excited states. Note that these plots have very similar form to the probability density in k space associated with the ground, first excited, and second excited states of a simple harmonic potential.

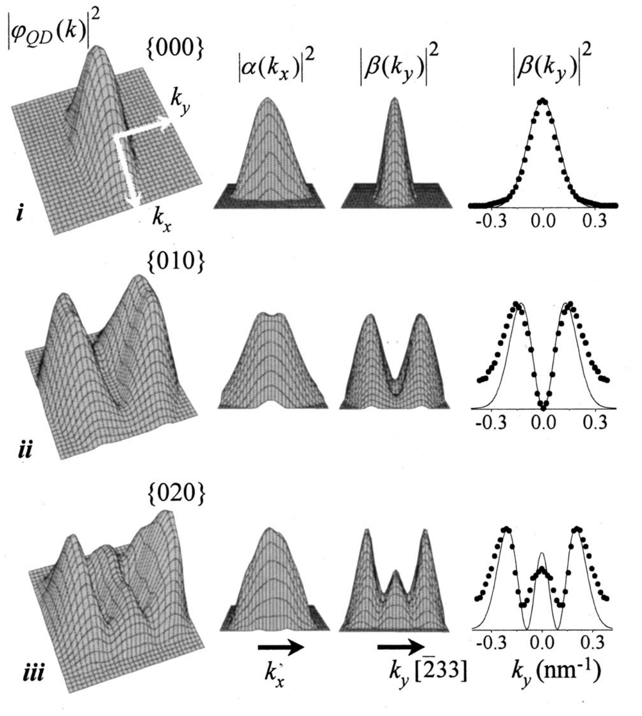

FIG. 5. Variation of the differential conductance, $G=dI/dV$, in the plane (k_x,k_y) for three representative states {000}, {010}, and {020} of quantum dots grown on a $(311)B$-oriented GaAs substrate (device A1). This provides a spatial map of $|\varphi_{\mathrm{QD}}(k_x,k_y)|^2$, the probability density in k space of the electron wave function of the QD. The form of $|\varphi_{\mathrm{QD}}(k_x,k_y)|^2$ along two distinct axes k_x and k_y is also shown. On the right-hand side of the figure, continuous lines show the wave-function probability in k space for the three lowest energy states of a harmonic oscillator with parameters determined by a fit to the $|\varphi_{\mathrm{QD}}(k_y)|^2$ data points (full circles).

For the magnetic field range used in our experiment ($0<B<12$ T), the in-plane magnetic field acts as only a weak perturbation on the dot states due to their strong confinement along z: for $B=12$ T, the quantum magnetic length $l_B=(\hbar/eB)^{1/2}$ is equal to ~ 8 nm, which is considerably larger than the electron confinement length along z ($l_z\sim 2$ nm). Hence the magnetotunneling probe acts as only a minor perturbation of the electron wave function in the dot. Further support for this conclusion is provided by the observed B dependence of the voltage position of the resonant peaks in $I(V)$ (see Fig. 4). All features in $I(V)$ show only a small quadratic shift ($\sim B^2$) to lower bias with increasing B, which is approximately the same for all resonances, and is consistent with the expected diamagnetic shift of the energy of the emitter states.

V. PROBING THE ELECTRON WAVE FUNCTION OF (311)*B* AND (100) QD'S

We use our magnetotunneling experiment to obtain two-dimensional maps of the probability densities of the electron states confined in the QD's. By plotting $G(B)$ for a particular

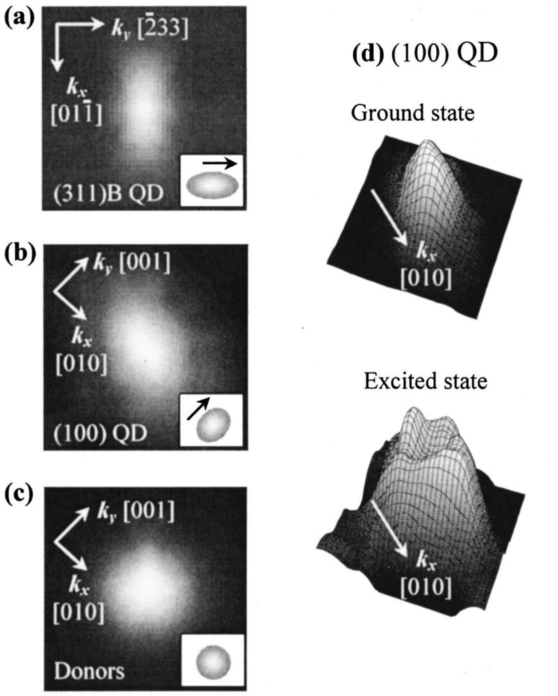

FIG. 6. Distribution in the (k_x, k_y) plane of the probability density, $|\varphi(k_x, k_y)|^2$, of the electron wave function for quantum dots grown on a (a) (311)B- and (b) (100)-oriented GaAs substrates and (c) for Si donors. The arrows indicate two main crystallographic directions on the (100)- and (311)B-oriented GaAs planes. The insets illustrate the form of the electron wave function in real space. (d) Plots of $|\varphi_{\mathrm{QD}}(k_x, k_y)|^2$ in the plane (k_x, k_y) for the ground and excited states of (100) quantum dots.

direction of B in the growth plane (x,y), we can measure the dependence of $|\varphi_{\mathrm{QD}}(k)|^2$ along the **k** direction perpendicular to B. Then, by making a series of measurements of $G(B)$ for various directions of B in (x,y), we can obtain the full, two-dimensional profile of $|\varphi_{\mathrm{QD}}(k_x, k_y)|^2$. This represents the **k**-space projection of the probability density of the electronic state confined in the QD.

Figure 5 shows the form of $G(B) \sim |\varphi_{\mathrm{QD}}(k_x, k_y)|^2$ in the plane (k_x, k_y) for the three representative QD states corresponding to resonances *i*, *ii*, and *iii* shown in Fig. 4 for sample A1. The contour plots of $|\varphi_{\mathrm{QD}}(k_x, k_y)|^2$ clearly reveal the characteristic form of the probability density distribution of a ground state orbital and the characteristic lobes of the higher energy states of the QD. It is clear from Fig. 5 that $|\varphi_{\mathrm{QD}}(k_x)|^2$ has approximately the same form for all three states, whereas $|\varphi_{\mathrm{QD}}(k_y)|^2$ corresponds to three lowest states of quantization along y. This suggests that, to a reasonable approximation, the probability density in **k** space, $|\varphi_{\mathrm{QD}}(k_x, k_y)|^2$, is separable, i.e., $|\varphi_{\mathrm{QD}}(k_x, k_y)|^2 = |\alpha(k_x)|^2 |\beta(k_y)|^2$. Although our measurements provide us with detailed information about the symmetry of the QD wave functions with respect to the in-plane coordinates, they give us no information about the z dependence. However, in general, the dot height is much smaller than the dimensions of the base. As the quantization energy of confinement along z is much higher than that for in-plane motion, in interpreting the magnetotunneling data, we assume that the motion along z is separable from the in-plane motion and that all the observed peaks involve final (QD) states that share the same type of quantum confinement along the z axis. This corresponds to the lowest energy quantization state for motion along z. This allows us to label the QD states using the quantum numbers n_x and n_y for the in-plane motion, and n_z for motion along z and to assign quantum numbers $\{n_x, n_y, n_z\} = \{000\}$, $\{010\}$, and $\{020\}$ to the states shown in Fig. 5.

The contour plots of $|\varphi_{\mathrm{QD}}(k_x, k_y)|^2$ reveal that the electron wave function has a biaxial symmetry in the growth plane, with axes corresponding within experimental uncertainty to the main crystallographic directions $[01\bar{1}]$ and $[\bar{2}33]$ in the (311)B plane. For the ground state, the probability density has a narrower distribution in **k** space along the $[\bar{2}33]$ direction than along $[01\bar{1}]$ [see Figs. 5 and 6(a)]. This indicates that the dot shape is anisotropic, with the wave function probability density elongated along the $[\bar{2}33]$ direction in real space.

Formation of anisotropic dots has been reported for $\mathrm{In}_x\mathrm{Ga}_{1-x}\mathrm{As}$ QD's grown on (311)B or (311)A GaAs substrates.[36–39] Anisotropy effects are more pronounced on the (311)A samples, where the bare (311)A-oriented GaAs surface reconstructs by forming an array of dimer rows elongated along the $[\bar{2}33]$ direction.[40,41] More recently, a similar reconstruction was also observed on the (311)B-oriented GaAs surface.[42,43] We suggest that the presence of dimer rows on the (311)B-oriented GaAs surface may act as a template for the subsequent growth of the strained material, and possibly generate a preferential direction for the dot nucleation.

Consistent with the anisotropic shape of the dot, the characteristic lobes of the first $\{010\}$ and second $\{020\}$ excited states are aligned along the elongated base of the dot (see Fig. 5), corresponding to the direction of lower quantization energy. The lobed structure of the first excited state resembles a p orbital in which the twofold degeneracy is lifted by the lowering of cylindrical symmetry induced by the anisotropic shape of the dot.

Our tunnel current measurements provide information about the wave-function probability density in **k** space, and we can determine the form of probability densities in real space if we approximate the $|\varphi_{\mathrm{QD}}(k_x, k_y)|^2$ plots by simple functions, e.g., the simple harmonic functions used to describe the form of the $|\beta(k_y)|^2$ plots of Fig. 5. For the ground state, $|\beta(k_y)|^2$ can be expressed as $\exp(-k_y^2 l_y^2)$, where l_y^2 is equal to the expectation value of y^2 ($l_y^2 = \langle y^2 \rangle$) and $k_y/B = e\Delta s/\hbar$. As discussed in Sec. III, the tunneling distance Δs may be different at different locations in the plane of the barrier due to mesoscopic effects in the emitter. For the dots that generate the strong resonances in the $I(V)$ plot, we estimate that Δs is in the range 20–28 nm. This leads to a corresponding uncertainty in the value of k_y/B ($=3-4 \times 10^7\ \mathrm{m}^{-1}\,\mathrm{T}^{-1}$) and in the size of the electron wave function, as estimated from the analysis of the $|\beta(k_y)|^2$ plots. We find that for the ground state $\{000\}$, $2l_y = 16 \pm 2$ nm, which is close to the typical in plane size of our (311)B dots ($\sim$18 nm) as measured by atomic force microscopy[44] and that $\langle y^2 \rangle$ increases with the quantum number n_y. A similar analysis for the $|\alpha(k_x)|^2$ plot allows us to determine the characteristic size of the electron wave function along *x*, $2l_x$, which is equal to 9 ± 1 nm.

The angular frequency of the oscillator, ω, is related to the lateral extent l of the wave function and to the electron effective mass m according to the relation $\omega = \hbar / ml^2$. This indicates that the quantization energy $\hbar\omega_x$ for electron motion along *x*, is significantly higher than that $(\hbar\omega_y)$ for motion along y $(\omega_x/\omega_y = l_y^2/l_x^2 \sim 3)$. The strong quantization of motion along the *x* axis may explain why we do not observe any resonant peak in $I(V)$ with a spatial form characteristic of a {100} state. First, such states should occur at an energy of $(3\hbar\omega_x/2) + (\hbar\omega_y/2) \sim 5\hbar\omega_y$, which exceeds the energy values of the {000}, {010}, and {020} states, approximately $2\hbar\omega_y$, $3\hbar\omega_y$, and $4\hbar\omega_y$, respectively. This means that the {100} states should occur in the voltage range (>0.1 V) over which the current starts to increase rapidly due to tunneling into the delocalized states of the wetting layer. This background current may well mask the resonant features corresponding to {100} states. Second, the stronger spatial localization of the {100} state means that the resonant current reaches a maximum value at a field of ~8 T compared to ~5 T for the {010} state. As discussed in further detail in Sec. VII and in the Appendix, at these higher fields the tunnel current is suppressed due to the effect of *B* on the transmission coefficient through the emitter barrier.

The in-plane anisotropy of the electron wave function is less pronounced for InAs QD's grown on a (100)-oriented GaAs substrate than for those grown on $(311)B$. Figure 6(b) shows plots of $|\varphi_{\mathrm{QD}}(k_x,k_y)|^2$ in the plane (k_x,k_y) for the ground state of (100) QD's (sample A2). The wave function has a biaxial symmetry in the growth plane, with axes corresponding quite closely to two main crystallographic axes, *x* and *y* ([010] and [001] axes). The wave function tends to be elongated along one crystallographic axis, but the anisotropic effects are less pronounced than for the case of $(311)B$ QD's. STM measurements on our uncovered QD's (with no GaAs cap layer) indicate that the dots tend to have a rectangular or square shape in the growth plane, with sides aligned along the [001] and [010] directions. Other groups also observed a similar alignment using STM, transmission electron microscopy, and atomic force microscopy techniques.[45,46] It has been proposed that ordering of dots along the [001] and [010] directions can be expected, as these directions correspond to the smallest stiffness constant of the crystal.[45] Also, a small misorientation of the GaAs substrate may cause symmetry breaking between the two directions and produce slightly anisotropic dot shapes, as suggested by our MTS images. For the excited state, the wave function exhibits a central node, i.e., it has a toroidal form, in contrast to the axial lobes that are found for the excited states of the $(311)B$ QD's [see Fig. 6(d)]. The different forms of the excited states for the two substrate orientations may originate from the different shape of the two types of dots. The pronounced anisotropic shape of the $(311)B$ dot leads to a preferential electron distribution along the elongated axis of the dot. In contrast, the more isotropic shape of the (100) dot leads to an approximately toroidal electron charge distribution for the first excited state, similar to that measured recently in spherical-shaped colloidal dots.[20]

For comparison purposes and as a means of validating the MTS technique, we have also studied the form of the electron wave function for hydrogenic-states associated with substitutional Si donors in a GaAs QW (sample C3). We used a $\mathrm{Al}_x\mathrm{Ga}_{1-x}\mathrm{As/GaAsAl}_x\mathrm{Ga}_{1-x}\mathrm{As}$ resonant tunneling diode in which the central plane of the quantum well was very lightly doped $(\sim 4 \times 10^9\ \mathrm{cm}^{-2})$ with Si donors.[26] In this case, it was shown[26] that an additional resonant peak is observed due to tunneling of electrons from the emitter into the $1s$ ground states of the QW-confined donors. This peak occurs at a bias close to the threshold for tunneling into the lowest energy subband of the QW. The $G(B)$ plots associated with tunneling into the ground state of the donors reveal that the electron wave function has circular symmetry in the growth plane, as expected for a $1s$ donor ground state [see Fig. 6(c)]. This result provides strong supporting evidence that the anisotropic wave functions of the dots [see Figs. 6(a) and 6(b)] are associated with their anisotropic shape, and not with any anisotropy of the quantum tunneling coefficient, as caused, for example, by the anisotropy of the conduction band structure of the $\mathrm{Al}_x\mathrm{Ga}_{1-x}\mathrm{As}$ tunnel barriers.[47]

With the simple two-terminal device used in our experiment, it is not possible to tell whether a particular ground state or first excited state resonance corresponds to resonant tunneling through the *same* QD or through two different QD's. In particular, resonances *i*, *ii*, and *iii* could correspond to states of different dots, albeit dots with a similar, laterally-confining potential. In Sec. VI, we describe a method of solving the problem of assigning the resonances to an individual dot.

VI. TUNNELING DIODES WITH ELECTROSTATIC GATES

We use a gating technology[33,48] to probe an ensemble of InAs QD's embedded within an $\mathrm{Al}_{0.2}\mathrm{Ga}_{0.8}\mathrm{As}$ tunnel barrier (sample B). Our device is a square mesa of side 0.7 μm, which incorporates four independent, lateral gates in addition to the source and drain contacts [see Fig. 2(b)]. Full details of the processing of tunneling diodes with electrostatic gates were given in Ref. 49. The active area of the device is reduced due to the finite extent of the Schottky depletion regions around the gates. This implies that for a dot density of $\sim 10^{11}\ \mathrm{dots/cm}^2$, there are fewer than 50 dots in the active region of the device.[33] Then, since the effect of the applied gate voltage, V_g, on an individual QD is to adjust its potential energy by an amount dependent on its proximity to the gates, the gate electrodes provide an electrostatic means of addressing a particular dot within the ensemble.

Figure 7(a) shows a gray-scale plot of the differential conductance *G* for the gated device, taken at a temperature of 0.3 K and at $B = 0$ T. The axes of the plot are the source-drain voltage, *V*, and gate voltage, V_g. The gate voltage is applied to two of the four gate electrodes. Lighter shading represents higher values of *G*. Resonances in the conductance are observed in the source-drain voltage range 0–0.3 V,

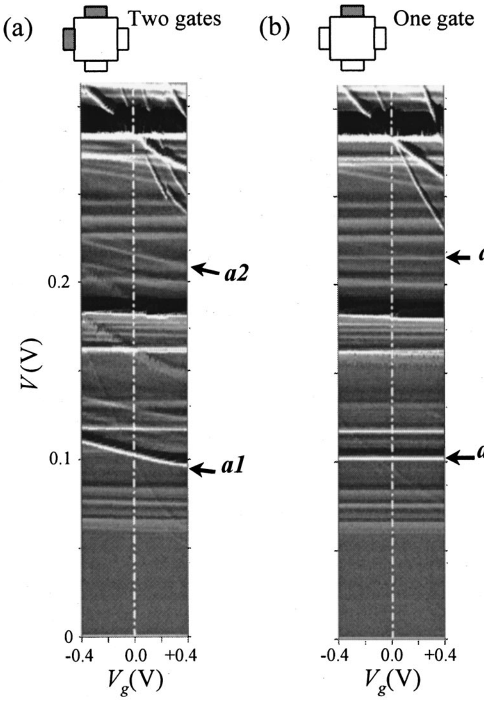

FIG. 7. Gray-scale plots of the differential conductance, $G = dI/dV$, at $T = 0.3$ K for device B. The axes are source-drain voltage V and gate voltage V_g. Lighter shading represents higher values of G. The negative gate voltage is applied on (a) two or (b) one of the four gate electrodes.

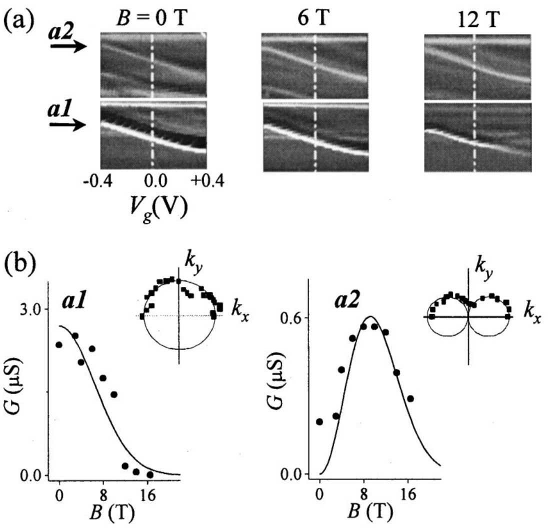

FIG. 8. (a) Gray-scale plots of the conductance, $G = dI/dV$, at $T = 0.3$ K, with axes of source-drain voltage V and gate voltage V_g for resonances $a1$ and $a2$ at $B = 0$, 6, and 12 T (device B). (b) B dependence of the amplitude of the peak in conductance associated with resonances $a1$ and $a2$ ($V_g = +0.4$ V). This provides a plot of $|\varphi_{\mathrm{QD}}(k)|^2$, the wave-function probability density in Fourier space of the electron confined in the dot. Continuous lines are fits to the measured $|\varphi_{\mathrm{QD}}(k)|^2$ using the probability density of the two lowest-energy states of a harmonic oscillator. The insets show two-dimensional maps of $|\varphi_{\mathrm{QD}}(k)|^2$ in the (k_x, k_y) plane. k_x and k_y are parallel to the main crystallographic directions of the (311)B plane, $[01\overline{1}]$ and $[\overline{2}33]$, respectively.

and are due to tunneling through the dots. The differential conductance peaks allow us to identify the onset of the resonance for each QD state, and to determine clearly the gate-voltage dependence of each resonant feature. The values of source-drain voltage, at which the resonant peaks occur, move at different rates with varying V_g. For those QD's that are closer to the two active gates, we can expect that the voltage position of the conductance resonances is more sensitive to V_g than for those that are remote from the gates. When one of the two gates is switched off, some of the resonances become independent of V_g, indicating that they arise from those dots further from the gate that is still active [see Fig. 7(b)]. Here we focus on two conductance peaks labeled $a1$ and $a2$. They exhibit an almost identical dependence on V_g, and also on the combination of gates used. This strongly suggests that $a1$ and $a2$ are due to tunneling through *different* quantum states of the *same* dot.

The nature of resonances $a1$ and $a2$ can be probed in further detail by magnetotunneling spectroscopy. Figure 8(a) shows gray-scale plots of G at $T = 0.3$ K and $B = 0$, 6, and 12 T in the voltage range of the two resonances. The magnetic field affects the voltage position of $a1$ and $a2$ in a similar way, while it affects their amplitude differently: increasing B to 6 T has the effect of increasing the intensity of resonance $a2$, whereas it decreases the intensity of $a1$. Detailed analysis of the $G(B)$ plots [see Fig. 8(b)] shows that resonance $a1$ has a maximum in $G(B)$ at $B = 0$ T followed by a steady decay to zero at around 10 T; resonance $a2$ shows almost no conductance at $B = 0$ T, with $G(B)$ increasing to a broad maximum at ~10 T, followed by a gradual decay to zero. Note that the magnetic field scale of the modulation of the $G(B)$ plots is higher than that observed in samples A1 and A2. This is a result of the different design of sample B; the smaller tunneling distance ($\Delta s \sim 10$ nm) implies that higher magnetic fields are required to probe the range of $\mathbf{k}$ vector associated with a given dot state ($k = eB\Delta s/\hbar$).

The different B dependence of the amplitude of the resonant features $a1$ and $a2$ suggests that they arise from different types of dot states, namely, the ground ($a1$) and the first ($a2$) excited state. The form of the two-dimensional maps of the electron probability densities also confirms this assignment. As can be seen in Fig. 8(b), the contour plots of $|\varphi_{\mathrm{QD}}(k_x, k_y)|^2$ reveal the characteristic form of the probability density distribution of a ground-state orbital ($a1$) and the characteristic lobes of the higher-energy state ($a2$) of the dot.

We now show that the measured probability density profiles are consistent with the measured energy spacing, ΔE, between the dot states associated with resonances $a1$ and $a2$. ΔE is determined by rescaling the voltage spacing $\Delta V \sim 114$ mV between the two resonances by the electrostatic leverage factor f, where $\Delta E = e\Delta V/f$. By using $f = 2.5 \pm 0.5$, estimated from a simple electrostatic model for the device, we find $\Delta E = 40-60$ meV. On the other hand, if we fit the measured value of $|\varphi_{\mathrm{QD}}(k)|^2$ by the calculated probability density for the ground and first excited states of a harmonic oscillator potential [see the continuous lines in Fig.

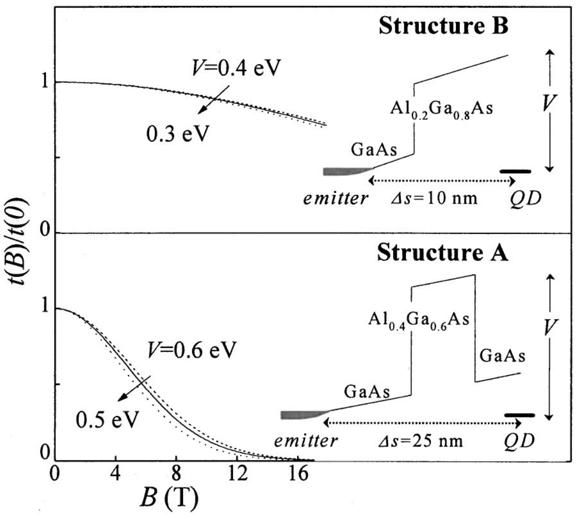

FIG. 9. Magnetic-field dependence of the transmission coefficient t of the tunneling barrier between the occupied emitter states and the QD layer for structures of types A (bottom) and B (top). The insets sketch the form of the tunneling barrier for the two types of structure. Δs and V describe, respectively, the tunneling distance and the height of the tunnel barrier at $B=0$ T. The transmission coefficient was calculated assuming a value of V equal to 0.6 V (dashed line), 0.55 V (continuous line), and 0.5 V (dotted line) for devices of type A, and equal to 0.4 V (dashed line), 0.35 V (continuous line), and 0.3 V (dotted line) for devices of type B.

8(b)], we find that the electron wave function in real space extends over a characteristic length $2l_0=14$ nm, which is comparable with the typical in-plane size of our dots (~18 nm).[44] Since the angular frequency of the oscillator, ω_0, is related to l_0 and to the electron effective mass m, we can obtain an independent estimate of ΔE according to the relation $\Delta E=\hbar\omega_0=\hbar^2/ml_0{}^2$. Assuming that the strain modified InAs effective mass is in the range $(0.03-0.04)m_e$, where m_e is the free-electron mass,[50,51] we find that $\hbar\omega_0=39-52$ meV, which is comparable with the measured value of ΔE.

VII. LIMITATIONS OF THE MTS TECHNIQUE

Although the MTS technique allows us to observe clear quantization effects in the dot, a direct correlation between the measured values of I and/or G, and the probability density plots may be limited by a number of factors. When an electron tunnels from the emitter into the QD, it can be scattered by the local distribution of impurities. This has the effect of broadening the range of k values acquired by the electron, thus limiting the "resolution" of the MTS technique in probing the detailed form of the probability density plots, such as the nodal features of the QD electron wave function. Note, for example, that the minimum of the second (*iii*) excited state of the dot does not correspond to zero as expected for a wave function node (see Fig. 5). In addition, the momentum gained by the electron in the (x,y) plane through the action of the Lorentz force also leads to a reduction in the energy associated with the motion along z. This is equivalent to an increase of the effective barrier height, which leads to a B-dependent suppression of the amplitude of the tail of the electron wave function in the emitter and a corresponding decrease of the transmission coefficient t with increasing B.[52] This effect can be described by expressing the tunneling current as $I\sim|MT|^2$, where T is the Bardeen transfer-matrix element between the emitter and the quantum dot states and $t=|T|^2$ (see the Appendix). In order to measure the Fourier transform (M) of a quantum dot wave function by measuring the B dependence of I, it is necessary that t is a constant or depends only weakly on B. Using the WKB approximation and the barrier parameters, we have estimated the B dependence of t. As shown in Fig. 9, the transmission coefficient and hence the current are reduced by a factor two at $B\sim6$ T in the type-A devices. This dependence is weaker than that experimentally observed for resonance *i* and differs qualitatively from the observed non-monotonous B dependence of resonances *ii* and *iii*: note that resonance *ii* (*iii*) actually *increases* in amplitude over the range of field 0 to 4 T (3–7 T) [see the right inset of Fig. 4(a)]. This indicates that the increase of effective barrier height due to B has a relatively small effect, and that the plots shown in Fig. 5 represent images of the actual probability density in k space of an electron state confined in the dot, slightly distorted by the B dependence of the transmission coefficient. In order to reduce this distortion, it would be desirable to reduce the B dependence of T relative to that of M, for example, by reducing the value of the tunneling distance Δs and/or by increasing the height of the tunneling barrier. This is realized in sample B, where the dots are embedded directly in a single $Al_{0.2}Ga_{0.8}As$ barrier and the tunneling distance is reduced to a value of ~10 nm, compared with $\Delta s=25$ nm for the type-A structures. As can be seen in Fig. 9, for sample B, the transmission coefficient depends weakly on B and it is reduced only by a factor 1.3, even at the maximum field used for this type of structure.

Finally, as a further development of the MTS technique, it would be desirable to reduce the uncertainty in the value of the tunneling distance, Δs, the parameter that controls the scale of k values $(k/B=e\Delta s/\hbar)$. This could be done by redesigning the emitter contact, e.g., by using a prewell in the emitter region. This would allows us to define more precisely the location of the wave function in the emitter and hence the value of Δs.

VIII. PROSPECTS AND CONCLUSIONS

In recent years, several different approaches have been used to calculate the eigenstates of QD's. They include perturbation theory, effective mass calculations,[8] eight-band $\mathbf{k}\cdot\mathbf{p}$ theory,[53,17,18] and empirical pseudopotential models.[19] Published work describing these calculations generally depicted the wave functions in the form of plots of the probability density in real space, $|\psi_{QD}(\mathbf{r})|^2$. Since it is a straightforward task to Fourier transform the calculated wave function into its $\mathbf{k}$-space equivalent, a direct comparison could then be made with our measured probability densities in $\mathbf{k}$ space. Also, we believe that the form of the probability densities may provide a useful means of assessing the confining potential of the dot. The shape and composition of the dots that are currently studied by optical and electrical measurements are not known precisely, so theoreticians deal with simple and ideal dot morphologies, with correspondingly simplified profiles for the dot potential.

We believe that MTS studies of the type reported here can now be extended to other material systems and interesting devices. In principle, by using appropriately designed devices with *p*-type contact layers, the MTS technique could be used to investigate the wave function of the holes. Also, the quantum states associated with ring-shaped QD's (Ref. 16) or with the many-body states of a QD could be investigated.[54]

In conclusion, we have shown that magnetotunneling spectroscopy provides a means of probing the electron wave function of self-assembled InAs QD's. We have identified confined states in the dot showing the elliptical symmetry of the ground state and the characteristic lobes of the excited states. We have also drawn a correlation between the spatial symmetry of the electron wave function and the morphological properties of quantum dots grown on differently oriented GaAs substrates. Finally, we have shown that the MTS technique can be further refined by using tunnel devices that incorporate gate electrodes. The gate technique was used as a means of identifying and measuring the energy levels and corresponding wave function probability densities of an individual dot.

ACKNOWLEDGMENTS

We acknowledge the support of the Engineering and Physical Sciences Research Council (United Kingdom) and the support of the Japan-U.K. collaboration project. E.E.V. and Y.D. gratefully acknowledge support from the Royal Society (United Kingdom). M.L.Z. acknowledges support from the Colciencias (Colombia). We gratefully acknowledge Dr. Y. Hirayama (NTT) for his support.

APPENDIX

We use a tunneling Hamiltonian approximation to model the effect of an in-plane magnetic field on the tunneling current through a quantum dot. This provides a simple theoretical framework for the MTS technique. The model calculation reveals some of the limitations of the technique that we have discussed in the main text.

We consider a resonant tunneling structure of the type shown in Fig. 1. In the experiment, the tunneling current along the growth direction (which is defined as the z direction) was measured in the presence of a magnetic field **B**, applied perpendicular to the z axis. In the experiment, **B** was applied along different directions in the xy plane, but without loss of generality we can choose the direction of **B** as the x axis in the following discussion.

We divide the system into three subsystems: emitter (E), quantum dot (QD), and collector (C). Each subsystem can then be described by an appropriate Hamiltonian H_S, where $S=E$, QD, or C. For the case in which the tunneling current I is limited by the emitter barrier, I is proportional to the modulus squared of the product of the tunneling matrix element M and the Bardeen transfer-matrix element T between the emitter and the quantum dot states, i.e., $I\sim|MT|^2$ where

$$M=\int\int \varphi^*_{\mathrm{QD}}(x,y)\varphi_E(x,y)dx\,dy \tag{A1}$$

and

$$T=\frac{\hbar^2}{2m}\left\{\chi_E(z)\frac{\partial\chi_{\mathrm{QD}}(z)}{\partial z}-\chi_{\mathrm{QD}}(z)\frac{\partial\chi_E(z)}{\partial z}\right\}_{z_0}. \tag{A2}$$

Here we assume separability between the xy and z motions of electrons. In these equations, $\Psi_S(x,y,z)=\varphi_S(x,y)\chi_S(z)$ is the eigenstate of H_S. T is evaluated at z_0, a point in the barrier between the emitter and the quantum dot layer.

The electronic states in the quantum dot are given by

$$H_{\mathrm{QD}}=\frac{1}{2m}(\mathbf{p}+e\mathbf{A})^2+U_{\mathrm{QD}}(x,y)+V_{\mathrm{QD}}(z), \tag{A3}$$

where U_{QD} and V_{QD} are the confining potentials in the xy plane and along z, respectively. Since **B** is applied parallel to the x axis, **A** can be written as $(0,-Bz,0)$ in the Landau gauge. For a quantum dot whose confining potential along z is much stronger than both the confining potential in the xy plane and the magnetic confinement, the quantum dot wave function $\Psi_{\mathrm{QD}}(x,y,z)$ may be written as the variational form

$$\Psi_{\mathrm{QD}}(x,y,z)=e^{iqy}\varphi^0_{\mathrm{QD}}(x,y)\chi^0_{\mathrm{QD}}(z), \tag{A4}$$

where q is a variational parameter and $\varphi^0_{\mathrm{QD}}(x,y)\chi^0_{\mathrm{QD}}(z)$ is the zero-field quantum dot state. The expectation value of H_{QD} for the wave function $\Psi_{\mathrm{QD}}(x,y,z)$ is then given by

$$\begin{aligned}\langle\Psi_{\mathrm{QD}}|H_{\mathrm{QD}}|\Psi_{\mathrm{QD}}\rangle=E^0_{\mathrm{QD}}+\tfrac{1}{2}m\omega_c^2[(l_B^2q-z_{\mathrm{QD}})^2\\ +\langle\chi^0_{\mathrm{QD}}|(z-z_{\mathrm{QD}})^2|\chi^0_{\mathrm{QD}}\rangle],\end{aligned} \tag{A5}$$

where $z_{\mathrm{QD}}=\langle\chi^0_{\mathrm{QD}}|z|\chi^0_{\mathrm{QD}}\rangle$ is the expectation value of z at $B=0$, $\omega_c=eB/m$, and $l_B=(\hbar/eB)^{1/2}$. By minimizing $\langle\Psi_{\mathrm{QD}}|H_{\mathrm{QD}}|\Psi_{\mathrm{QD}}\rangle$ with respect to the variational parameter q, we have $q=z_{\mathrm{QD}}/l_B^2$ and

$$\Psi_{\mathrm{QD}}(x,y,z)=e^{iyz_{\mathrm{QD}}/l_B^2}\varphi^0_{\mathrm{QD}}(x,y)\chi^0_{\mathrm{QD}}(z) \tag{A6}$$

$$E_{\mathrm{QD}}=E^0_{\mathrm{QD}}+\tfrac{1}{2}m\omega_c^2\langle\chi^0_{\mathrm{QD}}|(z-z_{\mathrm{QD}})^2|\chi^0_{\mathrm{QD}}\rangle. \tag{A7}$$

These equations clearly show that the magnetic field introduces an additional phase factor $\exp[i(z_{\mathrm{QD}}/l_B^2)y]$ into the wave function, and a diamagnetic shift of the electron energy.

For the three-dimensional states in the emitter, we have

$$\begin{aligned}H_E&=\frac{1}{2m}(\mathbf{p}+e\mathbf{A})^2+V_E(z)\\ &=\frac{p_x^2}{2m}+\frac{p_z^2}{2m}+\frac{(p_y-eBz)^2}{2m}+V_E(z).\end{aligned} \tag{A8}$$

Because both p_x and p_y commute with H_E, we can choose the wave function $\Psi_E(x,y,z)$ as

$$\Psi_E(x,y,z)=e^{ik_xx}e^{ik_yy}\chi_E(z). \tag{A9}$$

Inserting Eq. (A9) into Eq. (A8), $\chi_E(z)$ is found to satisfy the equation

$$\left[\frac{p_z^2}{2m}+V_E(z)+\frac{1}{2}m\omega_c^2(z-Z)^2\right]\chi_E(z)=\varepsilon\chi_E(z), \tag{A10}$$

where $Z=l_B^2k_y$ is the center coordinate of the magnetic confinement. The electron motion along z is determined by the electrostatic confining potential $V_E(z)$ plus the magnetic confinement $\frac{1}{2}m\omega_c^2(z-Z)^2$. Note that the center coordinate of the magnetic confinement is related to the wave vector along y through $Z=l_B^2k_y$.

Using the wave functions of the quantum dot and the emitter states given in Eqs. (A6) and (A9), the tunneling matrix element, M, is written as

$$\begin{aligned} M&=\int\int \varphi_{\mathrm{QD}}^*(x,y)\varphi_E(x,y)dx\,dy\\ &=\int\int \varphi_{\mathrm{QD}}^*(x,y)e^{ik_xx}\exp[i(k_y-z_d/l_B^2)y]dx\,dy\\ &=\varphi_{\mathrm{QD}}^0(k_x,k_y-z_{\mathrm{QD}}/l_B^2), \end{aligned} \tag{A11}$$

where $\varphi_{\mathrm{QD}}^0(k_x,k_y)$ is the two-dimensional Fourier transform of $\varphi_{\mathrm{QD}}^0(x,y)$. We define z_E as the coordinate of the edge of the Fermi sea of the electrons in the emitter (see Fig. 1). Electrons with orbits located at z_E, i.e., with $k_y\approx z_E/l_B^2$, will make the dominant contribution to the tunneling current, since states with $k_y\gg z_E/l_B^2$ (or $Z\gg z_E$) are empty and states with $k_y\ll z_E/l_B^2$ (or $Z\ll z_E$) are located deep inside the emitter, and therefore have lower probability of tunneling into the quantum dot. We therefore expect that the tunneling current is proportional to square of the Fourier transform of the quantum dot wave function,

$$\begin{aligned} I\propto|MT|^2&=\left|\varphi_{\mathrm{QD}}^0\left(k_x,\frac{z_E-z_{\mathrm{QD}}}{l^2}\right)\right|^2|T|^2\\ &=\left|\varphi_{\mathrm{QD}}^0\left(k_x,-\frac{eB\Delta s}{\hbar}\right)\right|^2|T|^2, \end{aligned} \tag{A12}$$

where $\Delta s=z_{\mathrm{QD}}-z_E$ is the tunneling distance along z. The tunneling current is given by integrating this equation over k_x according to the electron distribution in the emitter. Because $\mathbf{B}$ does not couple to the electron motion along x, the B dependence of I is mainly determined by the k_y dependence of the probability density in $\mathbf{k}$ space of the quantum dot wave function. Although Eq. (A12) is derived for three-dimensional emitter states, it can also be applied to weakly confined emitter states as long as the spatial confinement in xy plane in the emitter is much weaker than that in the quantum dot.

In order to measure the Fourier transform of a quantum dot wave function using Eq. (A12), it is necessary that T is a constant or depends weakly on B. The magnetic confinement along the z direction reduces the tunneling probability by increasing the effective barrier height at finite magnetic fields and thus reduces the tunneling current ($I\sim|T|^2$). Within the Wentzel-Kramer-Brillouin (WKB) approximation, the transmission coefficient $t=|T|^2$ can be expressed as $\exp[-(2/\hbar)\int_0^{\Delta s}\sqrt{2mV(z)}dz]$, where $V=V_E(z)+\frac{1}{2}m\omega_c^2(z-Z)^2$. Figure 9 shows the B dependence of t calculated for the barrier parameters of structures A and B.

---

*Present address: Universidad del Valle, Cali, Colombia.

[1] M. F. Crommie, C. P. Lutz, and D. M. Eigler, Nature (London) **262**, 218 (1993).
[2] J. F. Zheng, J. D. Walker, M. B. Salmeron, and E. R. Weber, Phys. Rev. Lett. **72**, 1490 (1994).
[3] S. H. Pan, E. W. Hudson, K. M. Lang, H. Eisaki, S. Uchida, and J. C. Davis, Nature (London) **403**, 746 (2000).
[4] K. L. McCormick, M. T. Woodside, M. H. Mingshaw Wu, P. L. McEuen, C. Duruoz, and J. S. Harris, Phys. Rev. B **59**, 4654 (1999).
[5] N. B. Zhitenev, T. A. Fulton, A. Yacoby, H. F. Hess, L. N. Pfeiffer, and K. W. West, Nature (London) **404**, 473 (2000).
[6] J. Y. Marzin, J. M. Gerard, A. Izraël, D. Barrier, and G. Bastard, Phys. Rev. Lett. **73**, 716 (1994).
[7] R. J. Nötzel, J. Temmyo, and T. Tamamura, Nature (London) **369**, 131 (1994).
[8] D. Bimberg, M. Grundmann, and N. N. Ledentsov, *Quantum Dot Heterostructures* (Wiley, New York, 1999), and references therein.
[9] D. Gammon, E. S. Snow, B. V. Shanabrook, D. S. Katzer, and D. Park, Science **273**, 87 (1996).
[10] A. P. Alivisatos, Science **271**, 933 (1996).
[11] S. A. Empedocles and M. G. Bawendi, Science **278**, 2114 (1997).
[12] L. Landin, M. S. Miller, M. E. Pistol, C. E. Pryor, and L. Samuelson, Science **280**, 262 (1998).
[13] Y. Toda, O. Moriwaki, M. Nishioka, and Y. Arakawa, Phys. Rev. Lett. **82**, 4114 (1999).
[14] U. Banin, Y. Cao, D. Katz, and O. Millo, Nature (London) **400**, 542 (1999).
[15] M. Bayer, O. Stern, P. Hawrylak, S. Fafard, and A. Forchel, Nature (London) **405**, 923 (2000).
[16] R. J. Warburton, C. Schaflein, D. Haft, F. Bickel, A. Lorke, K. Karrai, J. M. Garcia, W. Schoenfeld, and P. M. Petroff, Nature (London) **405**, 926 (2000).
[17] C. Pryor, M. E. Pistol, and L. Samuelson, Phys. Rev. B **56**, 10 404 (1997).
[18] W. Yang, H. Lee, T. J. Jonhson, P. C. Sercel, and A. G. Norman, Phys. Rev. B **61**, 2784 (2000).
[19] L-W. Wang, J. Kim, and A. Zunger, Phys. Rev. B **59**, 5678 (1999).
[20] O. Millo, D. Katz, Y. W. Cao, and U. Banin, Phys. Rev. Lett. **86**, 5751 (2001).
[21] R. Rinaldi, T. Johal, M. De Giorgi, A. Passaseo, and R. Cingolani, in *Proceedings of the 25th International Conference on the Physics of Semiconductors*, Osaka, Japan, edited by N. Miura and T. Ando (Springer-Verlag, Berlin, 2001).
[22] B. Grandidier, Y. M. Niquet, B. Legrand, J. P. Nys, C. Priester, D. Stievenard, J. M. Gerard, and V. Thierry-Mieg, Phys. Rev. Lett. **85**, 1068 (2000).
[23] E. E. Vdovin, A. Levin, A. Patanè, L. Eaves, P. C. Main, Yu. N.

Khanin, Yu. V. Dubrovskii, M. Henini, and G. Hill, Science **290**, 122 (2000).

[24] R. K. Hayden, D. K. Maude, L. Eaves, E. C. Valadares, M. Henini, F. W. Sheard, O. H. Hughes, J. C. Portal, and L. Cury, Phys. Rev. Lett. **66**, 1749 (1991).

[25] P. H. Beton, J. Wang, N. Mori, L. Eaves, P. C. Main, T. J. Foster, and M. Henini, Phys. Rev. Lett. **75**, 1996 (1995).

[26] J. W. Sakai, T. M. Fromhold, P. H. Beton, L. Eaves, M. Henini, P. C. Main, F. W. Sheard, and G. Hill, Phys. Rev. B **48**, 5664 (1993).

[27] A. Patanè, A. Polimeni, L. Eaves, P. C. Main, M. Henini, Yu. V. Dubrovskii, A. E. Belyaev, P. N. Brounkov, E. E. Vdovin, and Yu. N. Khanin, J. Appl. Phys. **88**, 2005 (2000).

[28] A. Patanè, A. Polimeni, L. Eaves, P. C. Main, M. Henini, A. E. Belyaev, Yu. V. Dubrovskii, P. N. Brounkov, E. E. Vdovin, and Yu. N. Khanin, Phys. Rev. B **62**, 13 595 (2000).

[29] M. Narihiro, G. Yusa, Y. Nakamura, T. Noda, and H. Sakaki, Appl. Phys. Lett. **70**, 105 (1997).

[30] I. E. Itskevich, T. Ihn, A. Thornton, M. Henini, T. J. Foster, P. Moriarty, A. Nogaret, P. H. Beton, L. Eaves, and P. C. Main, Phys. Rev. B **54**, 16 401 (1996).

[31] I. Hapke-Wurst, U. Zeitler, H. W. Schumacher, R. J. Haug, K. Pierz, and F. J. Ahlers, Semicond. Sci. Technol. **14**, L41 (1999).

[32] T. Suzuki, K. Nomoto, K. Taira, and I. Hase, Jpn. J. Appl. Phys., Part 1 **36**, 1917 (1997).

[33] D. G. Austing, S. Tarucha, P. C. Main, M. Henini, S. T. Stoddart, and L. Eaves, Appl. Phys. Lett. **75**, 671 (1999).

[34] P. C. Main, A. S. G. Thornton, R. J. A. Hill, S. T. Stoddart, T. Ihn, L. Eaves, K. A. Benedict, and M. Henini, Phys. Rev. Lett. **84**, 729 (2000).

[35] A. K. Geim, P. C. Main, N. La Scala, L. Eaves, T. J. Foster, P. H. Beton, J. W. Sakai, F. W. Sheard, M. Henini, G. Hill, and M. A. Pate, Phys. Rev. Lett. **72**, 2061 (1994).

[36] M. Kawabe, K. Akahane, S. Lan, K. Okino, Y. Okada, and H. Koyama, Jpn. J. Appl. Phys. **38**, 491 (1999).

[37] C. Lobo and R. Leon, J. Appl. Phys. **83**, 4168 (1998).

[38] P. O. Vaccaro, M. Hirai, K. Fujita, and T. Watanabe, J. Phys. D **29**, 2221 (1996).

[39] M. Henini, S. Sanguinetti, S. Fortina, E. Grilli, M. Guzzi, G. Panzarini, L. Andreani, M. Upward, P. Moriarty, P. Beton, and L. Eaves, Phys. Rev. B **57**, R6815 (1998).

[40] M. Wassermeier, J. Sudijono, M. D. Johnson, K. T. Leung, B. G. Orr, L. Däweritz, and K. Ploog, Phys. Rev. B **51**, 14 721 (1995).

[41] P. Moriarty, Y.-R. Ma, A. W. Dunn, P. H. Beton, M. Henini, C. McGinley, E. Mcloughlin, A. A. Cafolla, G. Hughes, S. Downes, D. Teehan, and M. Murphy, Phys. Rev. B **55**, 15 397 (1997).

[42] J. Marquez, L. Geelhaar, and K. Jacobi, Phys. Rev. B **62**, 9969 (2000).

[43] Z. M. Wang, L. Daweritz, and K. H. Ploog, Appl. Phys. Lett. **78**, 712 (2001).

[44] A. Polimeni, A. Patanè, M. Henini, L. Eaves, P. C. Main, S. Sanguinetti, and M. Guzzi, J. Cryst. Growth **201**, 276 (1999).

[45] G. E. Cirlin, G. M. Guryanov, A. O. Golubok, S. Ya. Tipissev, N. N. Ledentsov, P. S. Kop'ev, M. Grundmann, and D. Bimberg, Appl. Phys. Lett. **67**, 97 (1995).

[46] A. G. Cullis, A. J. Pidduck, and M. T. Emeny, J. Cryst. Growth **158**, 15 (1996).

[47] O. H. Hughes, M. Henini, E. S. Alves, M. L. Leadbeater, L. Eaves, M. Davies, and M. Heath, J. Vac. Sci. Technol. B **7**, 1041 (1989).

[48] M. W. Dellow, P. H. Beton, C. J. G. M. Langerak, T. J. Foster, P. C. Main, L. Eaves, M. Henini, S. P. Beaumont, and C. D. W. Wilkinson, Phys. Rev. Lett. **68**, 1754 (1992).

[49] D. G. Austing, T. Honda, and S. Tarucha, Semicond. Sci. Technol. **12**, 631 (1997).

[50] L. W. Wang, A. J. Williamson, A. Zunger, H. Jiang, and J. Singh, Appl. Phys. Lett. **76**, 339 (2000).

[51] M. A. Cusak, P. R. Briddon, and M. Jaros, Phys. Rev. B **54**, R2300 (1996).

[52] L. Eaves, K. W. H. Stevens, and F. W. Sheard, in *Proceedings of the Winter School Les Houches, France*, edited by M. J. Kelly and C. Weisbuch (Springer-Verlag, Berlin, 1986).

[53] O. Stier, M. Grundmann, and D. Bimberg, Phys. Rev. B **59**, 5688 (1999).

[54] S. Tarucha, D. G. Austing, T. Honda, R. J. vanderHage, and L. P. Kouwenhoven, Phys. Rev. Lett. **77**, 3613 (1996).